Effects of Amorphous and Nanocrystalline Structures on Hydrogen-Induced Optical Performance of Modulated Mg−Gd Films with Various Composition Fluctuations

Nanxiang Deng, Juan Chen,* Li-Ming Peng, Yue Liu, Yan Chen, Tianxing Lai, Wen-Jiang Ding, and Hong Zhu

ACCESS | Metrics & More | Article Recommendations

ABSTRACT: Nanomodification and amorphization are vital for improving the hydrogenation properties of magnesium (Mg)-based alloys. However, comparisons of their positive effects have been rarely presented because their usual fabrication process of annealing is hard to control. In this study, after tuning the composition fluctuation range, self-assembled well-ordered multilayer $Mg_{0.7}Gd_{0.3}$ films with an excessive amount of nanosized crystals were fabricated by deviating substrates to the edge of the sample stage, while relatively low crystallinity was gained at the center of the sample stage with a small composition fluctuation. It was demonstrated that the hydrogen diffusion rate in the sample deposited at the center with excessive amorphous regions was higher than that of the film fabricated at the edge with excessive nanocrystals regions. Besides, optical conversion ranges were monitored before and after the hydrogen absorption process. Films with large composition fluctuation possessed a high optical reflectance conversion range because the interference effects occurring inside improved their initial reflectance. However, films with small composition fluctuation inside gained a large transmittance conversion range due to their small nanostructured region.

KEYWORDS: Mg−Gd-modulated film, nanocrystalline, amorphous, magnetron co-sputtering, hydrogenation properties
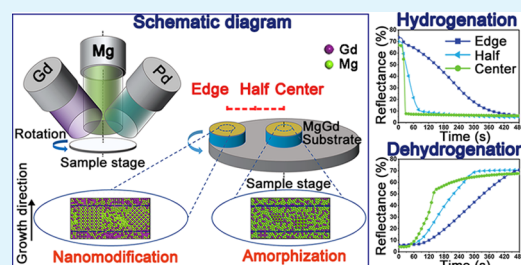
INTRODUCTION

Magnesium (Mg)-based materials are attractive as promising hydrogen storage materials in the future due to their natural abundance and high hydrogen storage capacity (nearly 7.6 wt %). However, their applications are limited due to their kinetics barrier and high operating temperature resulting from very stable thermodynamic properties.[1] Recently, significant research efforts have been devoted to circumvent the kinetics barrier-induced drawbacks by nanomodification and amorphization owing to high chemical activity and enhanced diffusion ability of hydride.[2,3]

Nanocrystal structural films have numerous interfaces that act as rapid diffusion pathways for hydrogen atoms.[4] Besides, nanomaterials have high surface energy and many lattice defects, which lower the dynamic barrier, improve the thermodynamic properties of Mg-based film, and lower the stability of the hydrides.[5] It has been reported that the diffusion rate of hydrogen atoms in grain boundary is often 2 or more orders of magnitude faster than the lattice diffusion.[6] Thus, the crystal size affects the hydrogen evolution performance of metal hydrides.[7−9]

Amorphization is also an effective strategy to accelerate the hydrogen diffusion inside bulk Mg by providing many internal defects as rapid diffusion pathways.[10−12] Amorphous $MgTi_x$
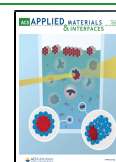
films were deposited with the ability to switch reversibly between the mirror and transparent states without an absorbing state due to the significant acceleration of hydrogen diffusion by amorphization.[10] Besides, reduction in the crystallization rate of Mg alloy films could improve the hydrogen storage capacities.[2] Moreover, Mg, Mg−Ni, and Mg−Cu amorphous films were deposited[12] by the sputtering method, which was found to be the best choice to deposit amorphous materials with supercooling rate.

Although the hydrogenation properties of Mg-based films can be improved by fabricating amorphous and nanostructure structures, the influence of these structures on the hydrogenation performance of Mg-based films has not yet been systematically studied. Furthermore, a comparison between the hydrogenation properties of films with different structures is of great significance and research value to explore the ideal structure so that hydrogen absorption and desorption proper-

ties of Mg-based films can be improved. It has been demonstrated that the crystallization rate of the films can mainly be tuned by two methods. One is annealing, which is a double-edged sword. On the one hand, after the annealing process, crystallization including nucleation and grain growth takes place in the amorphous film.[13] The films with Mg/Ni = 10:1 to 3.5:1 were X-ray amorphous when fabricated and then transformed to a crystalline structure after being annealed at 398 K.[12] It was reported that the Pd/Mg film exhibited improvement in its hydrogenation properties after the Mg layer was *in situ* annealed at 473 K for 2 h.[14] Besides, it was estimated that the Pd/Mg film could completely absorb hydrogen after treatment at 573 K.[15] However, structure evolution inside the Mg films during the annealing process has not been elucidated yet so that the scale of the nanostructured region is hard to control. On the other hand, the annealing process results in numerous side effects, including the formation of Pd−Mg intermetallic compounds between the Pd and Mg layer and the diffusion across the Mg/substrate interface.[6] Moreover, phase separation may take place upon annealing as reported for the Cu−Ta film, etc.[16,17] All of the factors mentioned above deteriorate hydrogenation properties. Taking these shortcomings into account, annealing is not suitable to modulate the crystallinity of the Pd/Mg-based film, thus searching for a new strategy is highly desirable and urgent.

The crystallization rate of the materials also strongly depends on the composition.[18] Matsuda et al. reported that Mg crystallization occurred in films with an initial Mg/Ni ratio of greater than 7.7, which was the eutectic composition between Mg and Mg_2Ni.[19] Akyıldız et al. fabricated $Mg_{95}Cu_5$ film with refined structures or $Mg_{90}Cu_{10}$ and $Mg_{85}Cu_{15}$ films, with X-ray amorphous region formed at 223 K.[12] However, these studies reported the change in the integral composition of the films, for which it was hard to form nanocrystals. Films with the same content ratio but different crystallinity can be fabricated by enlarging their composition fluctuation inside. Composition changes regularly in films along the film growth direction, and the amplitude of the composition modulation can be regulated in modulated alloy films. As a type of multilayered films, modulated alloy films can be deposited on a rotating substrate during co-sputtering from several confocal sources.[16,20−22] Process parameters of the assembling of the modulated structures, such as substrate rotation speed (given in rotations per minute (rpm)), deposition time, and target position at the sample stage have been discussed in some literature studies.[23,24] For instance, it was reported that the Cu/W modulated films with consecutive compositions could be deposited by tuning the position away from the center of the sample stage so that the distance between the sample and the targets during the sputtering process changes.[23] Besides, a series of Cu−Ta films were fabricated with the composition fluctuation ranging from 10 to 40 atom % regionally.[21]

Accordingly, it was hypothesized that if the composition fluctuation in films could be controlled, films with different crystallinity could be fabricated. Herein, films with lager area of nanocrystals can be correlated with the high degree of crystallinity, by enlarging the composition fluctuation in the Mg−Gd-modulated films, which were deposited by tuning the position away from the center of the sample stage so that the distance between the sample and the targets changed during the magnetron co-sputtering process. The microstructures were characterized by X-ray diffraction (XRD) to differentiate between phase and crystallinity. Moreover, aberration-

corrected transmission electron microscopy (TEM) was employed to analyze phases and grain sizes. The Mg−Gd films displayed detectable changes in optical properties upon hydrogen absorption; therefore, the optical properties and hydrogenation kinetics of fluorocarbon (FC)/Pd/Mg−Gd films with different degrees of crystallinity were examined simultaneously. We unveiled that films with a lower crystallization rate can absorb and desorb the hydrogen faster than the film with larger crystalline areas comprised of nanocrystals.

■ RESULTS AND DISCUSSION

Morphology and Structure Analysis. Herein, Pd (5 nm)/Mg−Gd (55 nm) thin films were fabricated by magnetron sputtering on glass substrates (Figure 1) at 5 rpm
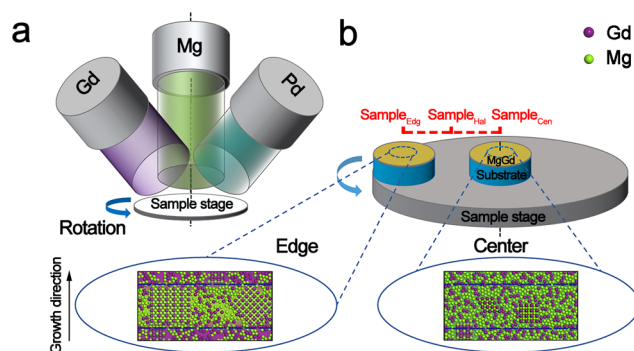
Figure 1. Mg−Gd films deposited by magnetron co-sputtering: (a) schematic illustration of the magnetron sputtering equipment and (b) deposition positions of films and schematic representation of the corresponding cross-sectional structures.

by modulating the sample positions: edge ($Sample_{Edg}$), half ($Sample_{Hal}$), and center ($Sample_{Cen}$). Figure 2 displays the surface morphologies and roughness degrees of $Sample_{Cen}$ and $Sample_{Edg}$. The reflectance of films is often relevant to surface roughness, and smoother surfaces can induce higher reflectance values. The root mean square roughness (rms, labeled as R_q) values of $Sample_{Cen}$ and $Sample_{Edg}$ were 0.409
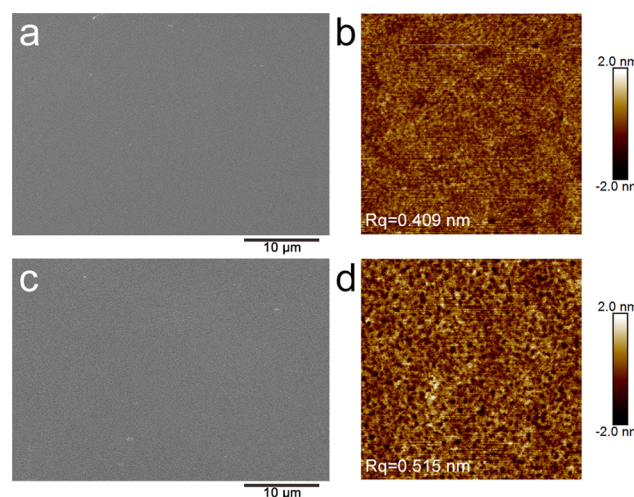

Figure 2. Surface morphologies of the Mg−Gd films without Pd and FC layers: scanning electron microscopy (SEM) and atomic force microscopy (AFM) images of (a, b) $Sample_{Cen}$ and (c, d) $Sample_{Edg}$.

and 0.515 nm, respectively, which indicated a small roughness difference estimated to be 0.1 nm that could be neglected in influencing their reflectance conversion range. The roughness values of Mg−Gd films were found to be smaller than that of Mg−Ni film (2 nm) with the same composition, which possessed lower reflectance conversion ranges.[25] Morphology of the films could be attributed to growth and grain size. According to "slowly diffusing element", Gd can suppress grain growth in Mg−Gd alloys.[26] Herein, the smoother surfaces of the Mg−Gd alloy films resulted from the smaller grain sizes of the Mg−Gd alloy films compared to the Mg−Ni alloy films.

Figure 3a shows the XRD results of Pd/Mg−Gd films, exhibiting the existence of peaks corresponding to Pd
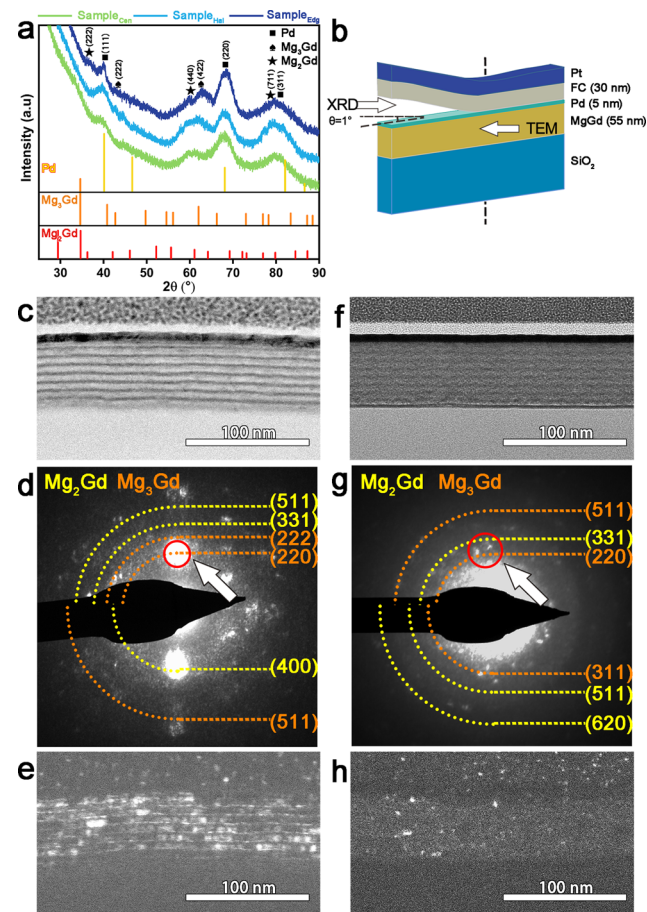
Figure 3. XRD patterns and TEM results of the as-prepared films: (a) XRD signal (only Pd/Mg−Gd layers); (b) schematic illustration of marked detection directions of XRD and TEM experiments; (c) BF, (d) microdiffraction pattern (only Mg−Gd layer), and (e) DF (taken from a spot marked in (d)) images of Sample$_{Edg}$; and (f) BF, (g) microdiffraction pattern (only Mg−Gd layer), and (h) DF (taken from spots marked in (g)) images of Sample$_{Cen}$.

(PDF#46-1043), Mg$_2$Gd (PDF#65-0039), and Mg$_3$Gd (PDF#65-0040) phases. The formation of Mg$_2$Gd and Mg$_3$Gd phases agreed well with the average composition of the Mg$_{0.7}$Gd$_{0.3}$ thin film. Besides, the XRD peaks of Sample$_{Edg}$ revealed a slightly higher crystallinity than Sample$_{Cen}$. Figure 3c shows a typical bright-field (BF) TEM image of Sample$_{Edg}$ with an obvious multilayered structure, which is blurred in the BF image of Sample$_{Cen}$ (Figure 3f). The dark-field (DF) TEM images shown in Figure 3e,h were captured using the diffraction spot outlined by the dashed circle in Figure 3d,g,

respectively. Moreover, the microdiffraction patterns of Sample$_{Edg}$ (Figure 3d) seemed more intensive than the diffraction rings of Sample$_{Cen}$ (Figure 3g), indicating the increase in crystallinity. Thus, it can be concluded that modulated films with different degrees of crystallinity can be deposited by changing the composition fluctuation inside. However, the results mentioned above were not enough to prove whether their grains were nanosized or not; thus, it was necessary to analyze their microstructure precisely even to figure out possible phases.

Detailed microstructural characterizations were also conducted. Figure 4a demonstrates the formation of a regularly distributed and multilayered Mg−Gd film when the sample was prepared at the edge. The TEM image reveals that the modulation period was around 7 nm, including a 5 nm Gd-poor layer and a 2 nm Gd-rich layer. Moreover, energy-dispersive spectrometry (EDS) line scan results demonstrated that Mg and Gd contents alternately changed along the growth direction, revealing parallel antiphase modulations. The composition fluctuation in Sample$_{Edg}$ suggested that Gd contents varied from 25 to 30% in Gd-poor layers to 30−35% in Gd-rich layers. Owing to the difference in modulated composition, variations in phase and crystallinity of different layers occurred.[27] Besides, it has been reported that the Mg−Gd alloys usually form several stable compounds, including MgGd, Mg$_2$Gd, Mg$_3$Gd, and Mg$_5$Gd. Therefore, when the content ratio of Mg/Gd ranged from 2.3 to 3 in Gd-poor layers, the Mg$_2$Gd and Mg$_3$Gd phases were likely to coexist in these layers. According to thermodynamic calculations, the formation enthalpy of Mg−Gd intermetallic compounds increased with the decrease in the Gd content. Thus, Mg$_3$Gd possessed lower enthalpy of formation than Mg$_2$Gd,[26,28] so it was more likely to stabilize in Gd-poor layers compared to Mg$_2$Gd. Considering this as a key point, the content ratio of Mg/Gd ranged from 1.86 to 2.3 in Gd-rich layers, indicating the facile generation of Mg$_2$Gd. Moreover, the interface between Pd and Mg−Gd alloy films appeared distinct, revealing that Gd-doping atoms served as buffer objects in suppressing the diffusion of Mg atoms.[29] This could improve the cycling stability and the optical performance during hydrogenation.[30,31]

Figure 4b shows the high-resolution TEM image, exhibiting a smooth transition in interface and composition between Gd-poor layers and Gd-rich layers. The fast Fourier transform (FFT, Figure 4c) results revealed region I in Figure 4b as hexagonal close-packed (hcp)-like structure with a lattice space of around 2.66 Å, corresponding to the [−1 −1 2 0] zone axis of Mg matrix crystals. On the other hand, despite the appearance of Mg matrix nanocrystals in the TEM image of Gd-poor layers, they were absent in the XRD data. Thus, the ratio of Mg matrix crystals would be very limited and their formation can be explained by irregular element distribution during the co-sputtering process.[16]

The nanocrystals in a Gd-poor layer were clearly observed by Cs-corrected scanning transmission electron microscopy (STEM, Figure 4d). The arrangement was consistent with the cubic structure viewed along the ⟨2 3 3⟩ zone axis (Figure 4e). Besides, the interatomic distances marked in Figure 4d were measured as 2.62 and 2.21 Å. Comparative analysis of the theoretical values of different Mg−Gd phases indicated that the measurement results excluded the existence of the Mg$_5$Gd and MgGd phases due to their distinctly different interatomic spacing. The interatomic spacing of Gd atoms in Mg$_2$Gd was
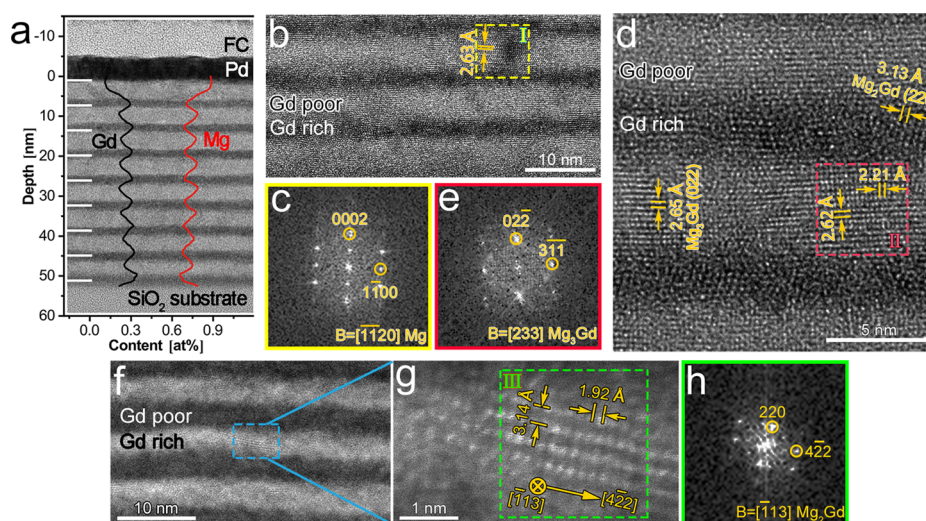
Figure 4. Microstructures of Sample$_{Edg}$: (a) TEM image as well as Mg and Gd line scanning results, (b) high-resolution TEM (HRTEM) image of Mg−Gd layer, (c) fast Fourier transform (FFT) image of region I in (b), (d) Cs-corrected HRTEM image, (e) FFT image of region II in (d), (f) Cs-corrected high-angle annular dark-field scanning transmission electron microscopy (HAADF-STEM) image, and (g) crystalline phase in Gd-rich layers corresponding to the inset square in (f), and (h) FFT image of region III in (g).

slightly larger than the interatomic distance measured and should not be neglected. Considering the accuracy of measurements, the experimental Gd−Gd distances seemed consistent with fcc Mg$_3$Gd, and as mentioned before, estimated composition and formation enthalpy of Mg−Gd made the Mg$_3$Gd phase more likely to exist in Gd-poor layers. Thus, Mg$_3$Gd could be proved to be the main component in Gd-poor layers. Moreover, the Cs-corrected HRTEM and diffraction pattern results confirmed the growth of Mg$_3$Gd nanocrystals along the [1 1 0] direction in the Gd-poor layers (Figure 4d,e). According to the TEM images (Figure 4b), it could be estimated that the Mg$_3$Gd phase showed an average grain size of around 10 nm in Sample$_{Edg}$, which corresponded to the grain size presented in the DF micrograph (Figure 3e).

Besides, obvious lattice fringes were clearly visible in Gd-poor layers, while they were difficult to identify in Gd-rich layers (Figure 4b). Nanocrystals in the Gd-rich layers were depicted clearly by high-angle annular dark-field imaging of scanning transmittance electron microscopy (HAADF-STEM; Figure 4f,g). These atomic analyses provided additional insights into the crystal structure. Considering the accuracy of measurements, the atomic arrangements revealed by Cs-corrected HAADF-STEM were well consistent with cubic structure viewed along the ⟨−1 1 3⟩ or ⟨2 −1 1⟩ zone axis. Atomically resolved HAADF-STEM images allow direct comparison of observations based on the crystal structures of the phases. The interatomic distances were measured as 3.14 and 1.92 Å. Although the interatomic distances of Gd atoms in fcc Mg$_2$Gd and Gd both satisfied the requirement, the content ratio in the Gd-rich layers indicated more possibility of the formation of the Mg$_2$Gd phase.

Furthermore, most Mg$_2$Gd nanocrystals showed a preferential orientation along [1 1 0] in the Gd-rich layers (Figure 4f). The structures in both Gd-rich and Gd-poor layers consisted of a few amorphous regions and large crystalline domains (Figure 4d). By measuring the areas of the amorphous and crystalline domains in the CS-corrected HR-STEM images, the percentage of the crystalline areas in Sample$_{Edg}$ was very high. Furthermore, the grain size of nanocrystals in Sample$_{Edg}$ was already proven to be no more

than 10 nm. Herein, it can be concluded that the Mg$_{0.7}$Gd$_{0.3}$ modulated layer with a high crystallization rate and amounts of nanocrystals as well as large composition fluctuation was fabricated in Sample$_{Edg}$.

Unlike microstructures of Sample$_{Edg}$, composition fluctuation in Sample$_{Cen}$ was small (EDS line scan, Figure 5a), thus
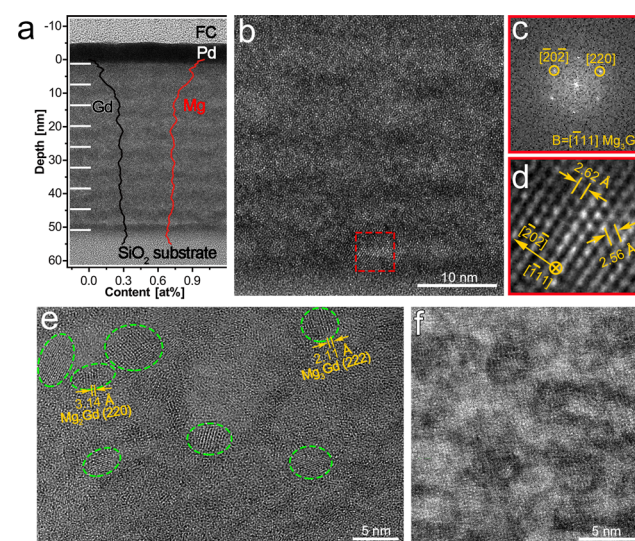
Figure 5. Microstructures of Sample$_{Cen}$: (a) TEM image, as well as Mg and Gd line scanning results; (b) HRTEM image of Mg−Gd layer; (c) FFT and (d) inverse FFT images of the square region in (b); (e) Cs-corrected HRTEM image. Nanocrystal regions were marked with cycles; and (f) Cs-corrected HAADF-STEM image.

modulated and multilayered structure was not obvious (marked with white line). Besides, Mg$_3$Gd and Mg$_2$Gd nanocrystals were visible in Figure 5b,e, in which the [1 1 0] orientation was not parallel to growth direction but grew randomly. The corresponding structure in Figure 5e shows that the film consisted of mainly amorphous domains and a few crystal sections. Furthermore, Mg and Gd elements seemed evenly distributed comparatively (Figure 5f). The percentages
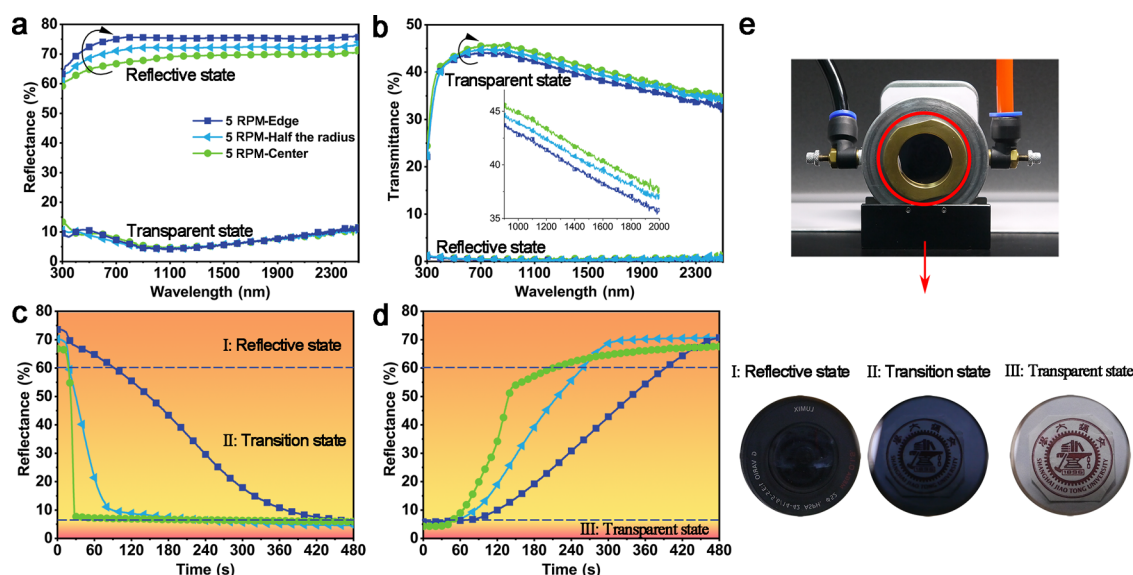
Figure 6. Typical optical properties measurements of FC/Pd/Mg−Gd films: (a) reflectance spectra and (b) transmittance spectra of the Mg−Gd alloy films, (c) hydrogenation and (d) dehydrogenation properties of FC/Pd/Mg−Gd films at the wavelength of 980 nm, and (e) setup used to characterize the optical properties of the as-obtained films. The optical color changes of films at different states are recorded using a camera, including metallic state (I), transition state (II), and transparent (III) state. The setup is placed in front of the logo "Shanghai Jiao Tong University".

of the crystalline areas in Sample$_{Cen}$ were estimated to be less than that in Sample$_{Edg}$ based on the measurement of the areas of the amorphous and crystalline regions in the CS-corrected STEM images. The composition was related to the degree of crystallinity of the films; therefore, a lower crystallization rate probably resulted from small composition fluctuation at this component ratio.[18,27] Thus, the Mg$_{0.7}$Gd$_{0.3}$ modulated layer with a low degree of crystallinity and large amorphous regions as well as small composition fluctuation were obtained in Sample$_{Cen}$.

Optical Properties of the FC/Pd/Mg−Gd Films. *Reflectance Conversion Range.* Figure 6a exhibits considerable variations in the reflectance properties upon hydrogenation. The increasing distance of the samples from the center led to the increased ratio of reflectance conversion range by about 10% (λ = 980 nm). The largest reflectance conversion range reached approximately 75% for Sample$_{Edg}$. As discussed earlier, films with smoother surfaces would have higher reflectance. Compared to the Mg−Ni films with the same content of Mg, Mg−Gd alloy films showed smoother morphologies and higher reflectance conversion ranges.[25] The small roughness differences among the Mg−Gd films fabricated at different positions probably induced no variation in reflectance. Therefore, improved reflectance values of Sample$_{Edg}$ might be mainly due to interference effects between layers.[32] This difference could be explained based on several factors: First, phases in Gd-rich and Gd-poor layers were distinct and stress obtained after sputtering was oriented along the layer, and this stress might contribute to higher reflectance.[33] Second, the modulated structure consisted of alternatively arranged Gd-rich and Gd-poor layers with different phases, which might induce different refractive indexes;[34,35] thus, the reflectance of the film would increase.[32,36] Third, the higher crystallization rate in Sample$_{Edg}$ might contribute to higher reflectance, as reported in GeSb.[37] Due to the complex structure of Mg−Gd modulated films,

more in-depth and comprehensive research would be needed to explain this optical difference.

Transmittance Conversion Range. Transmittance optical changes of FC/Pd/Mg−Gd films deposited at different positions are presented in Figure 6b. As deposition location was moved from the edge to the center, the ratio of transmittance in the transparent state increased slightly by about 4% and the largest transmittance conversion range reached ~44.6% for Sample$_{Cen}$. Several factors could explain these changes. First, mass grain boundaries existing in Sample$_{Edg}$ led to enlarged reflective index and scattering coefficient, contributing to lower transmittance.[38] Second, mass grains with different orientations inside Sample$_{Edg}$ caused reflection and scattering loss, thus lowering the transmittance.[39] Third, Sample$_{Edg}$ should have higher crystallinity, which resulted in elevated refractive rate and moderate transmittance.[40]

Hydrogenation and Dehydrogenation Process. Figure 6c shows the hydrogenation rates, revealing that Sample$_{Cen}$ was fully hydrogenated in a short time of 30 s, while Sample$_{Hal}$ and Sample$_{Edg}$ required 100 and 152 s, respectively. Upon loading of hydrogen, the reflectance of the FC/Pd/Mg−Gd films dropped down abruptly in region II and then slowly stabilized near the transparent state. The period with slow kinetics was ascribed to structural relaxation and an increase in internal stress upon reaching the hydrogen saturated state.[25,41]

The dehydrogenation process of the films was also carried out (λ = 980 nm) at room temperature and in the same chamber. Figure 6d demonstrates that Sample$_{Cen}$ regained its original reflectance in about 180 s, while Sample$_{Hal}$ and Sample$_{Edg}$ required 300 and 480 s, respectively. The dehydrogenation process can be explained based on the surface reactions occurring on Pd, where hydrogen was finally desorbed by forming water molecules with oxygen. The difference in hydrogenation and dehydrogenation rates can be explained based on several factors. First, Sample$_{Cen}$ seemed more uniform with a higher amorphous region, which

contributed to a superior hydrogen diffusion rate and a more diffusion path for hydrogen atoms, resulting in faster hydrogen absorption and desorption kinetics. In contrast, films with different crystallinities retained quite different hydrogenation properties.[2,10] Therefore, Sample$_{Edg}$ with lots of nanograins inside showed slower hydrogenation properties due to their higher degree of crystallinity.

Typical changes in the optical states of the films during the hydrogenation process were monitored using a camera,[42] and the results are illustrated in Figure 6e. The FC/Pd/Mg–Gd film showed metallic state at the beginning, followed by a blue transition state during the hydrogenation process and then full transparency when reaching saturated hydrogenation state. Rare earth (RE) metals can form hydrides with hydrogen at very low hydrogen pressures.[43] Therefore, the formation of the RE-hydride phase led to the separation of Mg, while maintaining the metallic state of the film. The appearance of such a transition state was associated with disproportionation into subwavelength size REH$_{2+\in}$ and Mg grains during the hydrogenation process.[44] Upon further loading, transparent MgH$_2$ was generated and served as a microscopic optical shutter. During hydrogenation of other Mg-based thin film layers, similar intermediate states were observed.[45−47]

Microstructural Diagram of Mg–Gd Film. The schematic illustration of Sample$_{Edg}$ is shown in Figure 7a. The Gd-rich layers and Gd-poor layers consisted of crystalline and amorphous heterostructures, respectively. The low ratio of

the Mg matrix nanocrystals led to a minor impact on the hydrogenation process.[8] Thus, this could be ignored and only Mg$_3$Gd and Mg$_2$Gd nanocrystal regions were depicted in Gd-poor and Gd-rich layers, respectively. Upon exposure to hydrogen, the Pd layer decomposed hydrogen into atoms, which then diffused across the Pd layer into the modulated Mg–Gd alloy layer, and then Gd atoms began to react. This resulted in the formation of the GdH$_2$ phases first,[48] followed by a gradual derivation of Gd from Mg$_3$Gd and Mg$_2$Gd phases. As the film became more exposed to hydrogen atoms, MgH$_2$ and GdH$_3$ were generated. During the hydrogenation process, the formation of MgH$_2$ in crystalline areas blocked further diffusion of hydrogen atoms, forcing them to diffuse through the amorphous region or grain boundaries. Besides, hydrogen atoms diffused in nanocrystals preferred to go through high index plane rather than being perpendicular to its close-packed plane.[1,49]

Figure 7b exhibits the existence of the Mg–Gd alloy structure with small composition fluctuations and few crystal regions. During hydrogen absorption and desorption processes, hydrogen atoms could diffuse rapidly and freely, improving the hydrogenation and dehydrogenation kinetics. Sample$_{Edg}$ revealed more Mg$_3$Gd and Mg$_2$Gd nanocrystals than those deposited at the center (Figure 3a). Formation of Mg$_3$Gd nanocrystals required more Mg atoms (Mg/Gd = 3:1) than average composition (Mg/Gd = 7:3), thus, higher Mg content in the Gd-poor layers met the composition requirement, forming more Mg$_3$Gd nanocrystals in the layer. Comparative analysis indicated that Mg$_2$Gd was likely to form on Gd segregation places in the Mg matrix,[50] appearing on the Gd-rich layers of Sample$_{Edg}$. In contrast, Mg$_3$Gd and Mg$_2$Gd nanocrystals were formed under composition fluctuation relatively evenly in the film prepared at the center.

Based on the above-mentioned discussion, Mg$_{0.7}$Gd$_{0.3}$ films with comprehensive and superior hydrogenation performances were formed, when all modulated alloy layers were amorphous (Figure 7c). These could be achieved by enhancing the cooling rate or lowering the sputtering temperature.[12] Modulated layers can improve the reflectance conversion range; therefore, the amorphous structure would enhance the transmittance conversion ranges and hydrogenation kinetics.

CONCLUSIONS

Co-sputtering method was employed for the synthesis of the Mg$_{0.7}$Gd$_{0.3}$ alloy layers with different crystallinity by simply changing the composition fluctuation by the deviation of the initial position of the samples from the center to the edge of the sample stage. The Mg$_{0.7}$Gd$_{0.3}$ layer deposited at the edge showed an obvious modulated layer structure with large composition fluctuation and large nanocrystalline domains, which were composed of fcc Mg$_3$Gd nanophases in Gd-poor layers and fcc Mg$_2$Gd nanocrystals in Gd-rich layers. The Mg$_{0.7}$Gd$_{0.3}$ film fabricated at the center showed lower crystallinity, which resulted from small composition fluctuation with relatively evenly distributed elements as well as large amorphous regions. It was found that the crystallization rate of the Mg–Gd layer plays a critical role in the hydrogen-induced optical properties of the FC/Pd/Mg$_{0.7}$Gd$_{0.3}$ modulated films. The FC/Pd/Mg$_{0.7}$Gd$_{0.3}$ modulated films with large amorphous regions in the Mg–Gd layer deposited at the center absorbed hydrogen quickly in only 30 s and desorbed hydrogen in 180 s. As the Mg–Gd layers further approached to the edge, reflectance conversion ranges of the FC/Pd/Mg$_{0.7}$Gd$_{0.3}$ films
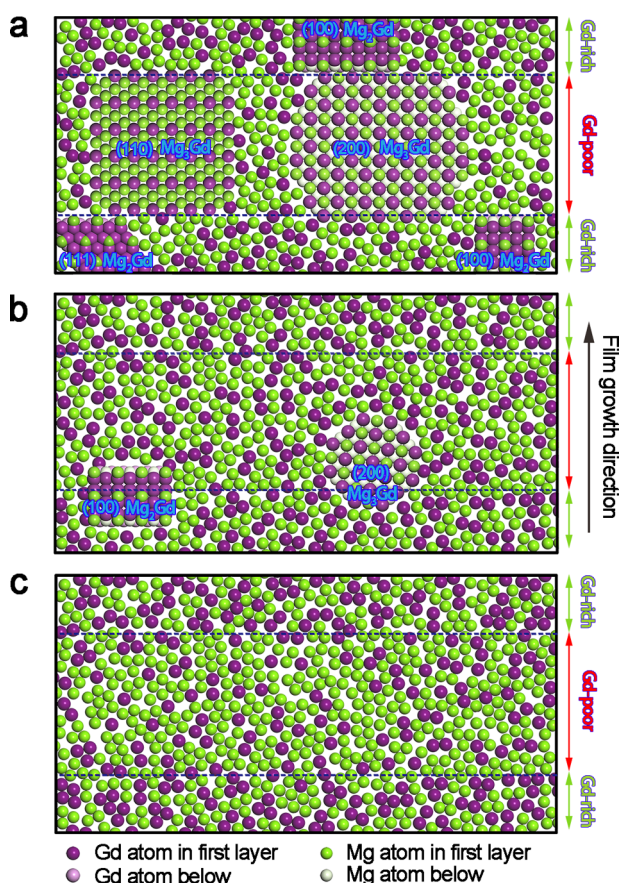
Figure 7. Schematic illustration of the atom distribution in the Mg–Gd film: (a) Sample$_{Edg}$ and (b) Sample$_{Cen}$ films deposited at 5 rpm and (c) ideal Mg–Gd film with the modulated structure containing mainly amorphous phase.

continuously enhanced by 10% and reached 75%, which was caused by interior interference of nanocrystals in the multilayer structure, while transmittance reduced by 4% and time required to form full hydrides prolonged by almost 5-fold. Therefore, films composed of an amorphous structure significantly improved hydrogenation and dehydrogenation kinetics than nanocrystalline ones. This study shows the possibility to tailor the thermodynamics of a metal−hydrogen system by changing the crystallization rate through composition fluctuation by the method of changing the sputtering position. Comprehensive studies are on-going to elucidate the influence of crystal size and number on the hydrogenation properties of the Mg−Gd films.

■ EXPERIMENTAL SECTION

Film Preparation. Pd/Mg−Gd films were first prepared using a magnetron sputtering apparatus (Denton Explore-14) composed of multiple sputter sources (Figure 1a). The magnetron sputtering apparatus was evacuated to a high vacuum with a background pressure of around 7.1×10^{-4} Pa. The targets were then presputter cleaned for 10 min prior to deposition. Considering the formation energy of Mg−Gd compounds and the related structural research of Mg−Gd,[26,28] $Mg_{0.7}Gd_{0.3}$ alloys were chosen, which was the average composition of Mg_2Gd and Mg_3Gd. To fabricate films with obviously different structures, $Mg_{0.7}Gd_{0.3}$ films were prepared by co-sputtering of Mg target under a 100 W direct current (DC) and Gd target with a 50 W DC power (Figure 1b). The purity of both targets approached 99.99 atom %. The radius (r) of the sample stage was set to ∼76.2 mm. Three films were prepared at 5 rpm by modulating the sample positions: edge ($Sample_{Edg}$, $r = 57.7$ mm), half ($Sample_{Hal}$, $r = 38.1$ mm), and center ($Sample_{Cen}$, $r = 0$ mm) as shown in Figure 1b. The selection of a relatively low rotation speed of 5 rpm was intended to induce more distinct differences both in structure and performance, as higher rotation speed would be inclined to eliminate the modulated structure.[51] During the co-sputtering process, the substrate at the center could receive sputtered atoms from three targets more evenly, while atoms sputtered unevenly on the edge with the periodic change in the distance between the substrate and targets. Herein, the structure of $Sample_{Edg}$ was modulated, while $Sample_{Cen}$ at the center was more uniform comparatively (Figure 1b). To catalyze hydrogen dissociation and protect the films from oxidation,[52] in situ capping with Pd layer (5 nm, 99.99 atom % purity) was performed with 100 W radio frequency (RF) power. Finally, a 30 nm FC polymer layer was fabricated by inductively coupled plasma chemical vapor deposition (ICP-CVD, SPTS) technique at room temperature using C_4F_8 as a reaction gas under 400 W power for 16 s, severely impeding the degradation of the film from condensed water.[53]

Structural Characterization. The thickness of each thin film was estimated using a KLA-Tencor P7 profilometer. Surface morphologies and roughness values were measured by scanning electron microscopy (SEM, Regulus8100) and atomic force microscopy (AFM, Dimension Icon & FastScan Bio). Chemical compositions were identified by SEM (Mira3) system equipped with an Aztec X-Max energy-dispersive spectrometer. Optical properties were detected using a spectrophotometer (Hitachi UH-4150) at the wavelength ranging from 300 to 2500 nm at room temperature with in situ hydrogen measurement facility. Films can gain large optical reflectance and transmittance conversion ranges at around 980 nm; hydrogenation kinetic responses and optical properties were recorded at this wavelength. The optical properties were measured from the substrate layer. Furthermore, hydrogenation investigations of the FC/Pd/Mg−Gd films were explored by keeping them under flowing 4% H_2 in Ar gas (200 sccm in 0.1 MPa), and the dehydrogenation process was carried out under air (300 sccm in 0.1 MPa) at room temperature. The hydrogen-induced optical performances of modulated Mg−Gd films were determined through multiple experiments. The microstructures and nanostructures were characterized by transmission electron microscopy (TEM, Talos F200X) operating at 200 kV

coupled with aberration-corrected STEM (JEOL JEM-ARM200F). It has to be mentioned that a region with obvious lattice fringes in the Cs-corrected HRTEM images was defined as a crystal. The percentages of the crystalline areas in the samples were estimated by measuring from the areas of the amorphous and crystalline regions in the CS-corrected HRTEM images. The crystallization rate was defined to be the ratio of the crystalline domains to the total area. TEM cross sections of the samples were prepared by applying a focused ion beam (FIB, *GAIA3 GMU Model 2016) system to films fabricated on thermal silicon oxide substrates. Pt layer was deposited as a protective layer to a free surface during the preparation process. The crystallinity and phase analyses were carried out by X-ray diffraction (XRD, Bruker D8 advance diffractometer).

■ AUTHOR INFORMATION

Corresponding Author

Juan Chen − National Engineering Research Center of Light Alloy Net Forming, State Key Laboratory of Metal Matrix Composites, Center of Hydrogen Science, and Materials Genome Initiative Center, Shanghai Jiao Tong University, Shanghai 200240, P. R. China; ⓘ orcid.org/0000-0001-5260-1631; Email: juanchen@sjtu.edu.cn

Authors

Nanxiang Deng − National Engineering Research Center of Light Alloy Net Forming, State Key Laboratory of Metal Matrix Composites, Shanghai Jiao Tong University, Shanghai 200240, P. R. China

Li-Ming Peng − National Engineering Research Center of Light Alloy Net Forming, State Key Laboratory of Metal Matrix Composites, Center of Hydrogen Science, and Materials Genome Initiative Center, Shanghai Jiao Tong University, Shanghai 200240, P. R. China

Yue Liu − National Engineering Research Center of Light Alloy Net Forming, State Key Laboratory of Metal Matrix Composites, Shanghai Jiao Tong University, Shanghai 200240, P. R. China

Yan Chen − National Engineering Research Center of Light Alloy Net Forming, State Key Laboratory of Metal Matrix Composites, Shanghai Jiao Tong University, Shanghai 200240, P. R. China

Tianxing Lai − School of Materials Science and Engineering, Shanghai Jiao Tong University, Shanghai 200240, P. R. China

Wen-Jiang Ding − National Engineering Research Center of Light Alloy Net Forming, State Key Laboratory of Metal Matrix Composites and Center of Hydrogen Science, Shanghai Jiao Tong University, Shanghai 200240, P. R. China

Hong Zhu − National Engineering Research Center of Light Alloy Net Forming, State Key Laboratory of Metal Matrix Composites, University of Michigan−Shanghai Jiao Tong University Joint Institute, and Materials Genome Initiative Center, Shanghai Jiao Tong University, Shanghai 200240, P. R. China; ⓘ orcid.org/0000-0001-7919-5661

Complete contact information is available at:
https://pubs.acs.org/10.1021/acsami.0c04694

Author Contributions

N.D. designed this experiment, fabricated the films, carried out hydrogenation properties, conducted structural analysis, and wrote the paper. J.C. researched literature, advanced the ideas, supervised the experiment, provided experimental technical guidance, and commented on and revised the manuscript. L.-M.P. researched literature, advanced the ideas, and discussed the manuscript. Y.L., Y.C., and T.L. prepared the samples and

conducted XRD experiment. W.-J.D. and H.Z. advanced the ideas.

■ **REFERENCES**

(1) Ouyang, L.; Tang, J.; Zhao, Y.; Wang, H.; Yao, X.; Liu, J.; Zou, J.; Zhu, M. Express Penetration of Hydrogen on Mg(1013) along the Close-Packed-Planes. *Sci. Rep.* **2015**, *5*, No. 10776.

(2) Zhao, Q. Y.; Li, Y. T.; Song, Y.; Cui, X. L.; Sun, D. L.; Fang, F. Fast Hydrogen-Induced Optical and Electrical Transitions of Mg and Mg-Ni Films with Amorphous Structure. *Appl. Phys. Lett.* **2013**, *102*, No. 161901.

(3) Uchida, H. T.; Kirchheim, R.; Pundt, A. Influence of Hydrogen Loading Conditions on the Blocking Effect of Nanocrystalline Mg Films. *Scr. Mater.* **2011**, *64*, 935−937.

(4) Kura, C.; Kunisada, Y.; Tsuji, E.; Zhu, C.; Habazaki, H.; Nagata, S.; Müller, M. P.; De Souza, R. A.; Aoki, Y. Hydrogen Separation by Nanocrystalline Titanium Nitride Membranes with High Hydride Ion Conductivity. *Nat. Energy* **2017**, *2*, 786−794.

(5) Alekseeva, S.; da Silva Fanta, A. B.; Iandolo, B.; Antosiewicz, T. J.; Nugroho, F. A. A.; Wagner, J. B.; Burrows, A.; Zhdanov, V. P.; Langhammer, C. Grain Boundary Mediated Hydriding Phase Transformations in Individual Polycrystalline Metal Nanoparticles. *Nat. Commun.* **2017**, *8*, No. 1084.

(6) Sunitha, Y.; Reddy, G. L. N.; Kumar, S.; Raju, V. S. Studies on Interdiffusion in Pd/Mg/Si Films: Towards Improved Cyclic Stability in Hydrogen Storage. *Appl. Surf. Sci.* **2009**, *256*, 1553−1559.

(7) Griessen, R.; Strohfeldt, N.; Giessen, H. Thermodynamics of the Hybrid Interaction of Hydrogen with Palladium Nanoparticles. *Nat. Mater.* **2016**, *15*, 311−317.

(8) Zhang, J.; Li, Z.; Wu, Y.; Guo, X.; Ye, J.; Yuan, B.; Wang, S.; Jiang, L. Recent Advances on the Thermal Destabilization of Mg-based Hydrogen Storage Materials. *RSC Adv.* **2019**, *9*, 408−428.

(9) Jeon, K. J.; Moon, H. R.; Ruminski, A. M.; Jiang, B.; Kisielowski, C.; Bardhan, R.; Urban, J. J. Air-Stable Magnesium Nanocomposites Provide Rapid and High-Capacity Hydrogen Storage without Using Heavy-Metal Catalysts. *Nat. Mater.* **2011**, *10*, 286−290.

(10) Fang, F.; Zhao, Q.; Wu, W.; Qiu, J.; Song, Y.; Cui, X.; Sun, D.; Ouyang, L.; Zhu, M. Achieving an H-induced Transparent State in 200 nm Thick Mg−Ti Film by Amorphization. *J. Appl. Phys.* **2014**, *115*, No. 014304.

(11) Beyer, W. Diffusion and Evolution of Hydrogen in Hydrogenated Amorphous and Microcrystalline Silicon. *Sol. Energy Mater. Sol. Cells* **2003**, *78*, 235−267.

(12) Akyıldız, H.; Öztürk, T. Hydrogen Sorption in Crystalline and Amorphous Mg-Cu Thin Films. *J. Alloys Compd.* **2010**, *492*, 745−750.

(13) Zhou, X.; Li, X. Y.; Lu, K. Enhanced Thermal Stability of Nanograined Metals below A Critical Grain Size. *Science* **2018**, *360*, 526−530.

(14) Qu, J.; Wang, Y.; Xie, L.; Zheng, J.; Liu, Y.; Li, X. Hydrogen Absorption−Desorption, Optical Transmission Properties and Annealing Effect of Mg Thin Films Prepared by Magnetron Sputtering. *Int. J. Hydrogen Energy* **2009**, *34*, 1910−1915.

(15) Gautam, Y. K.; Chawla, A. K.; Khan, S. A.; Agrawal, R. D.; Chandra, R. Hydrogen Absorption and Optical Properties of Pd/Mg Thin Films Prepared by DC Magnetron Sputtering. *Int. J. Hydrogen Energy* **2012**, *37*, 3772−3778.

(16) Müller, C. M.; Sologubenko, A. S.; Gerstl, S. S. A.; Spolenak, R. On Spinodal Decomposition in Cu−34at.% Ta Thin Films − An Atom Probe Tomography and Transmission Electron Microscopy Study. *Acta Mater.* **2015**, *89*, 181−192.

(17) Chen, H.; Zuo, J. Structure and Phase Separation of Ag−Cu Alloy Thin Films. *Acta Mater.* **2007**, *55*, 1617−1628.

(18) Ding, S.; Liu, Y.; Li, Y.; Liu, Z.; Sohn, S.; Walker, F. J.; Schroers, J. Combinatorial Development of Bulk Metallic Glasses. *Nat. Mater.* **2014**, *13*, 494−500.

(19) Matsuda, J.; Uchiyama, N.; Kanai, T.; Harada, K.; Akiba, E. Effect of Mg/Ni Ratio on Microstructure of Mg-Ni Films Deposited by Magnetron Sputtering. *J. Alloys Compd.* **2014**, *617*, 47−51.

(20) Hoummada, K.; Blum, I.; Mangelinck, D.; Portavoce, A. Composition Measurement of the Ni-Silicide Transient Phase by Atom Probe Tomography. *Appl. Phys. Lett.* **2010**, *96*, No. 261904.

(21) Müller, C. M.; Sologubenko, A. S.; Gerstl, S. S. A.; Süess, M. J.; Courty, D.; Spolenak, R. Nanoscale Cu/Ta Multilayer Deposition by Co-sputtering on a Rotating Substrate. Empirical Model and Experiment. *Surf. Coat. Technol.* **2016**, *302*, 284−292.

(22) Plantin, P.; Thomann, A. L.; Brault, P.; Renault, P. O.; Laaroussi, S.; Goudeau, P.; Boubeker, B.; Sauvage, T. Oscillating Composition of Fe−W Alloy Thin Films Grown by Magnetron Co-sputtering. *Surf. Coat. Technol.* **2007**, *201*, 7115−7121.

(23) Xie, T.; Fu, L.; Qin, W.; Zhu, J.; Yang, W.; Li, D.; Zhou, L. Self-assembled Metal Nano-multilayered Film Prepared by Co-sputtering Method. *Appl. Surf. Sci.* **2018**, *435*, 16−22.

(24) Pranevicius, L.; Wirth, E.; Milcius, D.; Lelis, M.; Pranevicius, L. L.; Bacianskas, A. Structure Transformations and Hydrogen Storage Properties of Co-sputtered MgNi Films. *Appl. Surf. Sci.* **2009**, *255*, 5971−5974.

(25) Slaman, M.; Dam, B.; Pasturel, M.; Borsa, D. M.; Schreuders, H.; Rector, J. H.; Griessen, R. Fiber Optic Hydrogen Detectors Containing Mg-based Metal Hydrides. *Sens. Actuators, B* **2007**, *123*, 538−545.

(26) Bugnet, M.; Kula, A.; Niewczas, M.; Botton, G. A. Segregation and Clustering of Solutes at Grain Boundaries in Mg−Rare Earth Solid Solutions. *Acta Mater.* **2014**, *79*, 66−73.

(27) Kajita, S.; Yamaura, S.-i.; Kimura, H.; Inoue, A. Hydrogen Sensing Ability of Pd-based Amorphous Alloys. *Sens. Actuators, B* **2010**, *150*, 279−284.

(28) Tang, B.; Wang, N.; Yu, W.; Zeng, X.; Ding, W. Theoretical Investigation of Typical FCC Precipitates in Mg-Based Alloys. *Acta Mater.* **2008**, *56*, 3353−3357.

(29) Paillier, J.; Bouhtiyya, S.; Ross, G. G.; Roue, L. Influence of the Deposition Atmosphere on the Characteristics of Pd-Mg Thin Films Prepared by Pulsed Laser Deposition. *Thin Solid Films* **2006**, *500*, 117−123.

(30) Bao, S.; Tajima, K.; Yamada, Y.; Okada, M.; Yoshimura, K. Metal Buffer Layer Inserted Switchable Mirrors. *Sol. Energy Mater. Sol. Cells* **2008**, *92*, 216−223.

(31) Yamada, Y.; Miura, M.; Tajima, K.; Okada, M.; Yoshimura, K. Influence on Optical Properties and Switching Durability by Introducing Ta Intermediate Layer in Mg−Y Switchable Mirrors. *Sol. Energy Mater. Sol. Cells* **2014**, *125*, 133−137.

(32) Weber, M. F.; Stover, C. A.; Gilbert, L. R.; Nevitt, T. J.; Ouderkirk, A. J. Giant Birefringent Optics in Multilayer Polymer Mirrors. *Science* **2000**, *287*, 2451.

(33) Kolle, M.; Lethbridge, A.; Kreysing, M.; Baumberg, J. J.; Aizenberg, J.; Vukusic, P. Bio-inspired Band-Gap Tunable Elastic Optical Multilayer Fibers. *Adv. Mater.* **2013**, *25*, 2239−2245.

(34) Liu, Y.; Daum, P. H. Relationship of Refractive Index to Mass Density and Self-Consistency of Mixing Rules for Multicomponent Mixtures Like Ambient Aerosols. *J. Aerosol Sci.* **2008**, *39*, 974–986.

(35) Young, J. C.; Finn, A. N. Effect of Composition and Other Factors on the Specific Refraction and Dispersion of Glasses. *J. Res. Natl. Bur. Stand.* **1940**, *25*, 759–782.

(36) Shuzhen, S.; Jianda, S.; Chunyan, L.; Kui, Y.; Zhengxiu, F.; Lei, C. High-Reflectance 193 nm Al_2O_3/MgF_2 Mirrors. *Appl. Surf. Sci.* **2005**, *249*, 157–161.

(37) Liu, C.; Cao, X.; Wang, J.; Yuan, Y.; Su, J.; Liu, C.; Cheng, L.; Zhang, X.; Li, J.; Zhang, X. Investigation on the Optical Phase Change Properties of Intrinsic GeSb and Ti-Doped GeSb. *Opt. Mater. Express* **2018**, *8*, 936–947.

(38) Dericioglu, A. F.; Kagawa, Y. Effect of Grain Boundary Microcracking on the Light Transmittance of Sintered Transparent $MgAl_2O_4$. *J. Eur. Ceram. Soc.* **2003**, *23*, 951–959.

(39) Tropf, W. J.; Thomas, M. E.; Harris, T. J. Properties of Crystals and Glasses. In *Handbook of Optics: Devices, Measurements and Properties*; McGraw-Hill: New York, 1995; Vol. 2, 33.7–33.12.

(40) Bahl, S. K.; Chopra, K. L. Amorphous Versus Crystalline GeTe Films. II. Optical Properties. *J. Appl. Phys.* **1969**, *40*, 4940–4947.

(41) Baldi, A.; Narayan, T. C.; Koh, A. L.; Dionne, J. A. In Situ Detection of Hydrogen-Induced Phase Transitions in Individual Palladium Nanocrystals. *Nat. Mater.* **2014**, *13*, 1143–1148.

(42) Liu, Y.; Chen, J.; Peng, L.; Han, J.; Deng, N.; Ding, W.; Chen, W. Improved Optical Properties of Switchable Mirrors Based on Pd/Mg-TiO_2 Films Fabricated by Magnetron Sputtering. *Mater. Des.* **2018**, *144*, 256–262.

(43) Schwartzkopf, M.; Santoro, G.; Brett, C. J.; Rothkirch, A.; Polonskyi, O.; Hinz, A.; Metwalli, E.; Yao, Y.; Strunskus, T.; Faupel, F.; Müller-Buschbaum, P.; Roth, S. V. Real-Time Monitoring of Morphology and Optical Properties during Sputter Deposition for Tailoring Metal–Polymer Interfaces. *ACS Appl. Mater. Interfaces* **2015**, *7*, 13547–13556.

(44) Giebels, I. A. M. E.; Isidorsson, J.; Griessen, R. Highly Absorbing Black Mg and Rare-Earth-Mg Switchable Mirrors. *Phys. Rev. B* **2004**, *69*, No. 205111.

(45) Baldi, A.; Pálsson, G. K.; Gonzalez-Silveira, M.; Schreuders, H.; Slaman, M.; Rector, J. H.; Krishnan, G.; Kooi, B. J.; Walker, G. S.; Fay, M. W.; Hjörvarsson, B.; Wijngaarden, R. J.; Dam, B.; Griessen, R. Mg/Ti Multilayers: Structural and Hydrogen Absorption Properties. *Phys. Rev. B* **2010**, *81*, No. 224203.

(46) Chen, Y.; Duan, X.; Matuschek, M.; Zhou, Y.; Neubrech, F.; Duan, H.; Liu, N. Dynamic Color Displays Using Stepwise Cavity Resonators. *Nano Lett.* **2017**, *17*, 5555–5560.

(47) Ngene, P.; Radeva, T.; Slaman, M.; Westerwaal, R. J.; Schreuders, H.; Dam, B. Seeing Hydrogen in Colors: Low-Cost and Highly Sensitive Eye Readable Hydrogen Detectors. *Adv. Funct. Mater.* **2014**, *24*, 2374–2382.

(48) Manassen, Y.; Realpe, H.; Schweke, D. Dynamics of H in a Thin Gd Film: Evidence of Spinodal Decomposition. *J. Phys. Chem. C* **2019**, *123*, 11933–11938.

(49) Das, S. K.; Kang, Y.-B.; Ha, T.; Jung, I.-H. Thermodynamic Modeling and Diffusion Kinetic Experiments of Binary Mg–Gd and Mg–Y Systems. *Acta Mater.* **2014**, *71*, 164–175.

(50) Li, Y.; Wang, J.; Chen, K.; Shao, M.; Shen, Y.; Jin, L.; Zhu, G.-z. Self-Patterning Gd Nano-Fibers in Mg-Gd Alloys. *Sci. Rep.* **2016**, *6*, No. 38537.

(51) Müller, C. M.; Sologubenko, A. S.; Gerstl, S. S. A.; Suess, M. J.; Courty, D.; Spolenak, R. Nanoscale Cu/Ta Multilayer Deposition by Co-Sputtering on A Rotating Substrate. Empirical Model and Experiment. *Surf. Coat. Technol.* **2016**, *302*, 284–292.

(52) Sanger, A.; Kumar, A.; Chauhan, S.; Gautam, Y. K.; Chandra, R. Fast and Reversible Hydrogen Sensing Properties of Pd/Mg Thin Film Modified by Hydrophobic Porous Silicon Substrate. *Sens. Actuators, B* **2015**, *213*, 252–260.

(53) Nugroho, F. A. A.; Darmadi, I.; Cusinato, L.; Susarrey-Arce, A.; Schreuders, H.; Bannenberg, L. J.; da Silva Fanta, A. B.; Kadkhodazadeh, S.; Wagner, J. B.; Antosiewicz, T. J.; Hellman, A.; Zhdanov, V. P.; Dam, B.; Langhammer, C. Metal–Polymer Hybrid Nanomaterials for Plasmonic Ultrafast Hydrogen Detection. *Nat. Mater.* **2019**, *18*, 489–495.